Journal of Molecular Structure 1317 (2024) 139201

Contents lists available at ScienceDirect

Journal of Molecular Structure

journal homepage: www.elsevier.com/locate/molstr

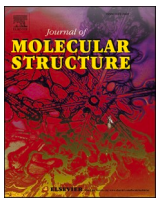

SHG behavior of the solid isomorphic compounds Ni- and Cu-5,10,15,20-tetraphenylporphyrinate. An experimental and theoretical study

Alma Cioci [a,*], Paola Antoniotti [a,b], Paola Benzi [a,b], Carlo Canepa [a], Elena Cariati [c,a], Enzo Laurenti [a], Domenica Marabello [a,b]

[a] Dipartimento di Chimica, University of Torino, Torino, Italy
[b] Crisdi – Interdepartmental Center for Crystallography, University of Torino, Torino, Italy
[c] Dipartimento di Chimica, University of Milano, Milano, Italy

ARTICLE INFO

Keywords:
Metal porphyrinates
SHG properties
Theoretical calculations
NLO properties
Structure-properties relashionship
Biosensors

ABSTRACT

We prepared and investigated the SHG behavior in the solid state of the two isomorphic Nickel and Copper 5,10,15,20-tetraphenylporphyrinate, that crystallize in the same acentric $I\bar{4}2d$ space group. The compounds were synthesized and characterized, and the Second Harmonic Generation (SHG) response of powdered samples was measured employing a 1.907 μm pulsed laser radiation. During laser irradiation, for both compounds, a gradual increase of the intensity of the SH signal was observed until, after a few minutes, it reached a plateau of about fifty times (for the Ni-TPP) or ten times (for the Cu-TPP) the initial value. We attempted to understand the origin of this phenomenon both through experimental analysis and theoretical calculations. Absorption and vibrational spectroscopies, in solution and solid state, combined with powder X-ray diffraction, both before and after irradiation, do not evidence any chemical degradation, phase transition or amorphization process. Theoretical calculations on little fragments of the Ni/Cu-TPP structure simulate appropriately the structural features of the complexes and their initial experimental SHG response. Magnetic balance measurement in the solid state before and after irradiation, in conjunction with DFT/B3LYP optimization of excited spin states and TDDFT calculations, highlight a change in the electronic and/or spin state due to the irradiation of the complexes.

1. Introduction

Bio-imaging experiments provided many structural, functional and mechanistic insights into biological processes at different levels of organization: tissue, cellular, and subcellular levels [1]. In particular, two-photon microscopy [1–3], of which Second Harmonic Generation (SHG)-based microscopy is an example, revolutionized the bio-imaging field by enabling non-invasive, high-resolution imaging of living samples in real time [4]. SHG microscopy is used in several applications, for example in probing cell–cell interactions, in scrutinizing cellular morphology, and even in recording waves of electrochemical activity of neurons in real time [1,2,5]. Moreover, since the observed signal scales with the square of the intensity of the incident light, the SHG microscopy provides excellent spatial resolution [4].

The SHG microscopy requires suitable nanoprobes, i.e. nanoparticles able to generate an SH signal at exactly half the wavelength of the incoming radiation [4]. Contrary to the probes that exploit fluorescence, since the signal is based on scattering rather than absorption, the SHG probes neither bleach nor blink, and the signal does not saturate with increasing illumination intensity [6]. This in principle permits to follow a biological process for a long time and, for this reason, the SHG-based nanoprobes are successfully employed for biological *in vitro* [7–10] and *in vivo* imaging [11].

In the last decades, for biological applications of SHG microscopy, several organic molecules were studied, since they are more biocompatible with respect to inorganic compounds. In order to obtain high sensitivity and resolution in SHG microscopy, molecules with an electron-density distribution that can be highly distorted under the influence of an optical field (high hyperpolarizabilities) are required [4]. Unfortunately, the organic molecules studied to date generally show only modest hyperpolarizabilities, limiting their use in bio-imaging.

Porphyrins are macrocyclic heterocyclic organic compounds that were widely studied as biosensors, due to their fluorescence properties [12–15]. Porphyrins possess a prominent π-electron delocalization,

* Corresponding author.
E-mail address: alma.cioci@unito.it (A. Cioci).

https://doi.org/10.1016/j.molstruc.2024.139201
Received 9 May 2024; Received in revised form 22 June 2024; Accepted 2 July 2024
Available online 3 July 2024

which can achieve a significant enhancement of hyperpolarizability by metal insertion at the ring center or by functionalization of the molecule at the peripheral positions [22]. For this reason, they show also interesting Non Linear Optical (NLO) properties, particularly Second (SHG) and Third (THG) Harmonic Generation in solution or encapsulated in polymers [16–20] and were already considered for NLO bio-imaging [21,22]. At our knowledge, up to now the SHG behavior of porphyrins and their derivatives at the solid state was not studied in depth.

Mandatory for a crystalline material to display the SHG property, is the absence of the inversion center in the crystal structure and also to eschew some special combination of symmetry elements [23].

In our previous work [24], we studied the SHG behavior of powdered samples of the Cobalt 5,10,15,20-tetraphenylporphyrinate (Co-TPP), that crystallizes in the acentric I$\bar{4}$2d space group. We observed a peculiar response, *i. e.* during a Nd:YAG pulsed laser irradiation a gradual increase of the intensity of the SH signal was observed, until it reached a plateau of about fifty times the initial value. The enhancement of the SHG efficiencies of the Co-TPP complex is imputable to an electronic or spin transition, that occurs when the Co-porphyrinate is irradiated.

In order to enhance the comprehension of the phenomenon, in this work we decided to study the SHG behavior of Nichel- and Copper-5,10,15,20-tetraphenylporphyrinates (NiTPP and CuTPP, respectively, Scheme 1), that are isomorphous (i.e. same crystal structure) with CoTPP and show the same peculiar SHG behavior.

We synthesized and characterized the two compounds with single crystal (XRD) and powder (XRPD) X-ray diffraction, UV–Vis, and IR spectroscopy in solution and solid state, EPR spectroscopy, magnetic balance, and we measured the SHG response of powdered samples with a 1.907 μm pulsed laser radiation. Furthermore, theoretical calculations were performed at the B3LYP/ 6–31G(d) level of theory on fragments of the crystal structure, in order to estimate the first-order static hyperpolarizability and second order susceptibility, that are correlated to the SHG response. The TDDFT method was also applied to the same systems, and the results were compared to the electronic spectra of the complexes.

2. Experimental

2.1. Synthesis of Nickel(II)- and Copper(II)-5,10,15,20-tetraphenylporphyrinate (Ni-TPP and Cu-TPP)

All solvents and raw materials were used as received from commercial suppliers (Sigma-Aldrich and Alfa Aesar) without further purification.

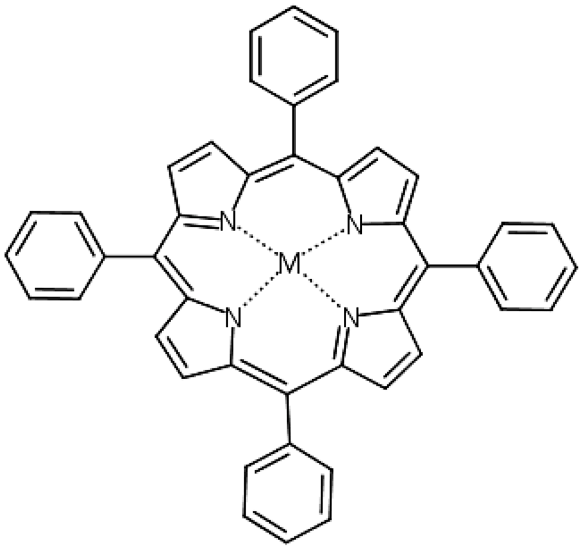

Scheme 1. Chemical scheme of M-5,10,15,20- tetraphenylporphyrinate (*M*=Ni/Cu).

Ni-TTP and Cu-TPP were synthesized according to the method reported by Girolami et al. [25]. The powder obtained was purified by dissolution in dichloromethane and re-crystallization through partial evaporation of the solvent. The crystalline powder was filtered and washed with a few drops of dichloromethane. The purity of the compounds was checked by absorption (Fig. S4 in Supplementary materials), vibrational- spectroscopies, and powder X-ray diffraction (XRPD).

2.2. Single crystal X-ray diffraction (XRD)

The crystals suitable for XRD were obtained by slow evaporation of the dichloromethane solution. X-ray diffraction data were collected at room temperature using the Atlas S2 Rigaku-Oxford Diffraction Gemini R-Ultra diffractometer equipped with using the mirror monochromatized Cu-Kα (1.5418 Å) radiation. The CrysAlisPro package [26] was used for data collection and integration, SHELXT [27] for resolution, SHELXL [28] for refinement and Olex2 [29] for graphics. Hydrogen atoms were found in the difference Fourier maps, nevertheless they were calculated and refined with riding coordinates and fixed U_{iso}at 1.2 times of the U_{eq} of the connected C atoms.

The interested reader can find further details on crystal data, data collection, least-squares refinements and CIF files (CCDC 2130188–2130189) in the Supplementary materials (Tables S1, S2, Figs. S1–S3).

2.3. Powder X-ray diffraction (XRPD)

The Powder X-ray diffraction patterns (XRPD) were collected with the same diffractometer of the XRD data collection. The powders were prepared by mixing 3.00 mg of each Ni-TPP and Cu-TPP sample with 0.50 mg of ZnO and the solid mixture was ground in an agate mortar. Then it was compacted with paraffin oil and modelled as a ball of ca. 0.45 mm diameter (less than the diameter of the X-ray beam). Each ball was glued on a glass capillary and mounted on the goniometer head of the instrument. Each powder pattern was collected by rotating the samples 60°, and with an exposure time of 60 s.

2.4. Absorption and vibrational spectroscopies

For the optical characterization of the Ni-TPP and Cu-TPP complex, UV–Vis absorption spectra were recorded on a Cary60 spectrometer using dichloromethane solutions ($10^{-}5$ M). Moreover, diffuse reflectance UV–Vis spectra of the powdered Ni-TPP and Cu-TPP were recorded by an Agilent Cary 100 UV–Vis spectrophotometer equipped with an integration sphere.

Attenuated total Reflectance-Fourier-Transform-Infrared (ATR-FTIR) spectra of the powdered Ni-TPP and Cu-TPP were recorded on a Cary 630 spectrophotometer.

2.5. Magnetic balance and electron paramagnetic resonance (EPR)

Magnetic susceptibility measurements were carried out with the Johnson Matthey Magnetic susceptibility Balance using Evans' method.

EPR spectra of solid Ni-TPP and Cu-TPP before and after irradiation were recorded at 77 K in a X-band Bruker-EMX instrument equipped with a cylindrical cavity operating at 100 kHz field modulation (microwave frequency 9.3 GHz, microwave power 10 mW, modulation amplitude 6 Gauss).

2.6. Computational methods

The calculations were performed with the GAUSSIAN16 program [30–32]. All geometries were optimized by gradient-based techniques [33,34] with no symmetry constraints at the DFT B3LYP level of theory

[35], in conjunction with the 6–31G(d) basis set for the C, H, and N atoms [36]. For Ni and Cu the LANL2DZ basis was used [37]. All critical points were characterized as energy minima by calculating their analytical frequencies. The total dipole moment, polarizability, and the first order hyperpolarizability were calculated at the same level of theory.

Since ab initio volume calculations based on numerical Monte Carlo integration introduce a large degree of error, to compute the molar volume in a more quantitative way, tight convergence in the self-consistent field procedure and increased density of points for more accurate integration were employed, and ten different volume calculations on the optimized geometries at the B3LYP level of theory with the options scf=tight, volume=tight, and iop(6/45=500,6/46=1) were averaged [38]. To explain the SHG behavior of the irradiated complex, we employed the time-dependent density functional theory (TD-DFT) [39, 40] with the same functional and basis set used for describing the excited states. In order to analyze the shapes of the molecular orbitals, the Gaussview 6.0 [41] was used.

2.7. SHG measurements

The SHG efficiency was determined by the Kurtz–Perry powder technique, [42] using a nanosecond Nd:YAG pulsed (10 Hz) laser, whose 1.064 μm fundamental wavelength was shifted to 1.907 μm by stimulated Raman scattering in a high-pressure hydrogen cell. The SH signal generated by ground samples in capillary tubes was collected by an elliptical mirror, detected by a photomultiplier, and compared to the ground sucrose signal collected in the same conditions (sucrose displays an SHG equal to 0.7 that of KDP in the same conditions).

3. Results and discussion

3.1. SHG measurements

Powders of Ni-TPP and Cu-TPP were ground separately in an agate mortar for a long time, in order to obtain solid particles of the same dimension, and thus limiting differences on the SHG response due to the crystal dimension. The same mechanical process was performed on powders of sucrose, the substance used as a standard in SHG measurements. All the ground powders were sealed into different capillaries and irradiated with the 1.907 μm pulsed laser radiation, to measure the SHG efficiency with respect to the sucrose. As already observed for Co-TPP [24], the initial efficiency of the two samples was of the same order of the sucrose, but after few seconds under laser irradiation it gradually increased, reaching a plateau at approximately fifty times for Ni-TPP and ten times for Cu-TPP of the initial value. Thus, the final intensity of Ni-TPP is similar to Co-TPP, while that of Cu-TPP is one fifth lower.

By visually analyzing the powders in the capillaries of both Ni-TPP and Cu-TPP, a darker spot was observed in correspondence of the point where the laser hit the samples, as already observed for Co-TPP. By repeating the measurement on the same spot, the SH intensity is equal to the value of the plateau for both compounds, and it remains stable for a long time (it has been regularly checked for two months). However, by moving the capillary to the not-irradiated powder, the same behavior of increasing of SHG under irradiation was again observed. Furthermore, we also noticed that the powders blew up into the capillary during the laser irradiation, especially for the NiTPP compound.

In order to understand the origin of this phenomenon, first of all we investigated the possibility of a photodegradation, and/or a phase transition and/or an amorphyzation process.

3.2. UV–Vis spectroscopies in the solid state

In order to investigate a possible photodegradation process, UV–Vis absorption spectra before and after irradiation were recorded. Since the investigated porphyrinates show the SHG peculiar property in the solid state, we performed this analysis on powdered material, without any modifications of the sample before the laser irradiation.

Fig. 1 shows the UV–Vis spectrum obtained by the powder of Ni-TPP. The y-axis shows the magnitude F(R). The figure was originally recorded as a percentage of reflectance and has a negative value compared to the reference. F(R) is directly proportional to the Kubelka–Munk function and is the inverse of (1—reflectance), so it is easily comparable to the absorbance reported for data in solution. The main peaks of Ni-TPP are found at 350, 520, and 619 nm. Instead of an intense band between 380 and 500 nm, there are two peaks at 350 and 427 nm. This splitting may depend on the interaction between two or more molecules of the crystalline aggregate, which results in two or more excitonic transitions with high transition moments [43–45].

Fig. 2 shows the UV–Vis spectrum obtained by the powder of Cu-TPP. The main peaks are found at 350, 530, and 629 nm. Again, instead of an intense band in the region between 380 and 500 nm, there are two peaks at 350 and 472 nm.

Figs. 1 and 2 also reported the comparison between the powder before (black lines) and after (red lines) the irradiation described in the previous section. As it is possible to notice, in the solid state the UV–Vis absorption spectra show no significant changes, both in the number and in the wavelength of the bands after the irradiation, as opposite to the Co-TPP, exhibiting some differences. In fact, we noticed that for the Co-TPP the darker color of the spot after irradiation is a permanent condition, while for Ni-TPP and Cu-TPP the darker spots disappeared after few seconds, and thus a variation of the UV–Vis spectra could not be expected.

3.3. ATR-FTIR spectroscopies in solid state

The ATR-FTIR spectra of Cu/Ni-TPP, both before and after irradiation, are shown in Figs. 3 and 4. All the principal expected bands, as predicted from previous studies [46,47] have been detected.

For both complexes, the 3020–3051 range is visible the absorptions of CH stretching of the phenyl groups. The two spectra, in the range between 1500 and 600 cm^{-1} showed many bands, which reflect the complexity of porphyrin ring. Particularly, for NiTPP (Fig. 3) the bands between 413 and 466 cm^{-1} are attributable to in-plane rotational motion of the pyrrole rings, including the wagging of the phenyl groups. For Cu-TPP (Fig. 4) the corresponding bands are red shifted, and are located at 408–443 cm^{-1}. For Ni-TPP, the bands between 517 and 557 cm^{-1} are attributable to out-of-plane skeletal deformation of the phenyl groups, and the corresponding bands for Cu-TPP are in the same range (522–560 cm^{-1}). For Ni-TPP, the bands between 650 and 695 cm^{-1} are attributable to the expansion of the phenyl groups. In the same range we find the corresponding bands for Cu-TPP. For both complexes, the bands between 710 and 834 cm^{-1} are attributable to the wagging of the H atoms of both the phenyl groups and the macrocycle. The band at 1006 cm^{-1} (for Ni-TPP) or at 1004 cm^{-1} (for Cu-TPP) is attributable to the in-plane bending deformation of the phenyl rings. For both complexes, at 1070 cm^{-1} we find a band attributable to the rocking of the H atoms on the C atoms on the ring. The band attributable to the in-plane structural deformation of the pyrrole ring is found at 1350 cm^{-1} for Ni-TPP and 1344 cm^{-1} for Cu-TPP. The band attributable to the rocking of the H atoms on the phenyl rings and to the symmetric stretching of the two opposite C-C bonds in the C-C-C units is found at 1400 cm^{-1} for both complexes. No differences are detectable, both in the number and in the wavelength of the bands, before and after irradiation, confirming the results of UV–Vis analysis.

3.4. Powder X-ray diffraction (XRPD)

Since the photo-degradation phenomenon was ruled out by the spectroscopic characterization, we considered a possible phase transition or a partial amorphization of the powders under the laser beam. The formation of a different crystalline phase after irradiation would change

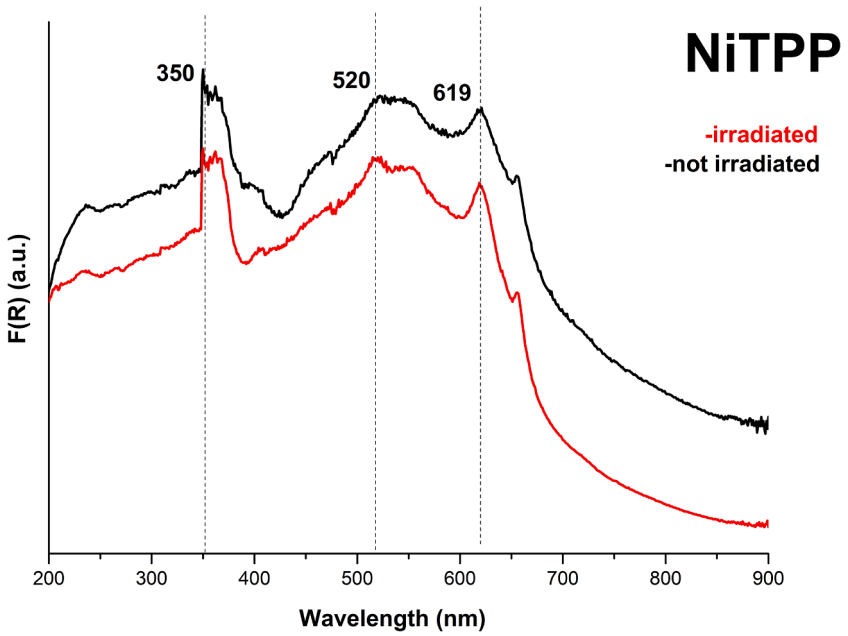

Fig. 1. UV–Vis absorption spectra of solid Ni-TPP before and after irradiation.

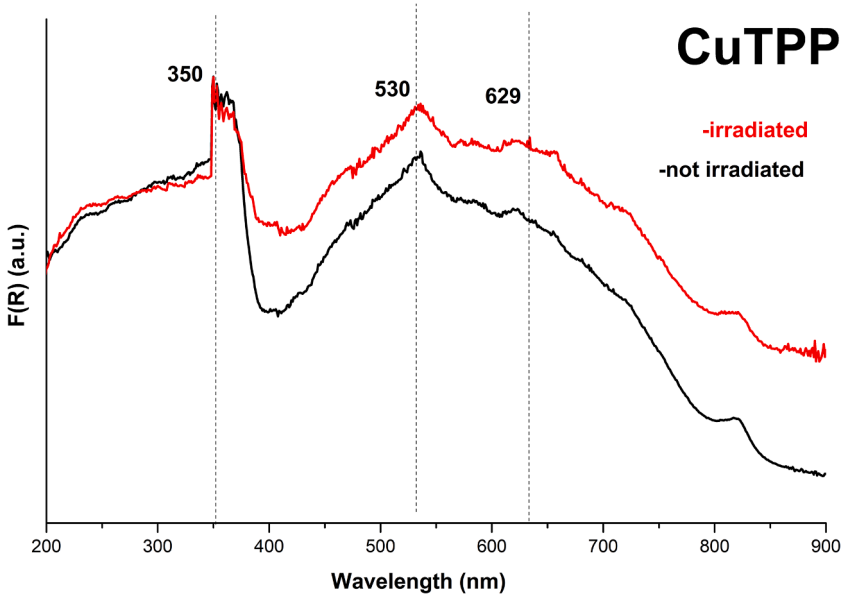

Fig. 2. UV–Vis absorption spectra of solid Cu-TPP before and after irradiation.

completely the peaks positions and intensities in the powder patterns, while the amorphization process would reduce the intensities with respect to a standard and, possibly, widen the peaks. In Fig. 5 are reported the XRPD patterns of the powders both before and after irradiation, compared to the XRPD patterns calculated from the XRD structures; in each powder sample, an equal amount of ZnO as standard was mixed, and the patterns were scaled on its higher intense peak. Fig. 5 shows that no differences between patterns before and after irradiation can be observed, leading to the conclusion that no structural modifications or partial amorphization of the samples can be considered, as already shown for the CoTPP sample. Furthermore, these results indicate a strong chemical and structural stability of the porphyrinates to the irradiation with the high power pulsed laser beam, and that also in these cases we have to investigate the eventuality of an electronic and/or spin state induced by the laser beam.

In order to further investigate a possible imperceptible variation of the structure, we attempted to irradiate a single crystal of Ni-TPP and Cu-TPP, but, as in the case of Co-TPP, the crystals under examination blew up quite immediately after the irradiation, and they were divided into many crystalline fragments that were scattered in the capillary.

3.4.1. Magnetic balance

The magnetic moments of Ni- and CuTPP were determined with the magnetic balance before and after irradiation on three M-TPP samples, irradiated in different times. In addition, for each sample five different measurements were made on one of the irradiated samples at intervals of one week.

For the NiTPP compound, the results of the measurements on the non-irradiated samples are consistent with the literature data, [48] that determined it to be a singlet. Instead, the irradiated Ni-TPP samples

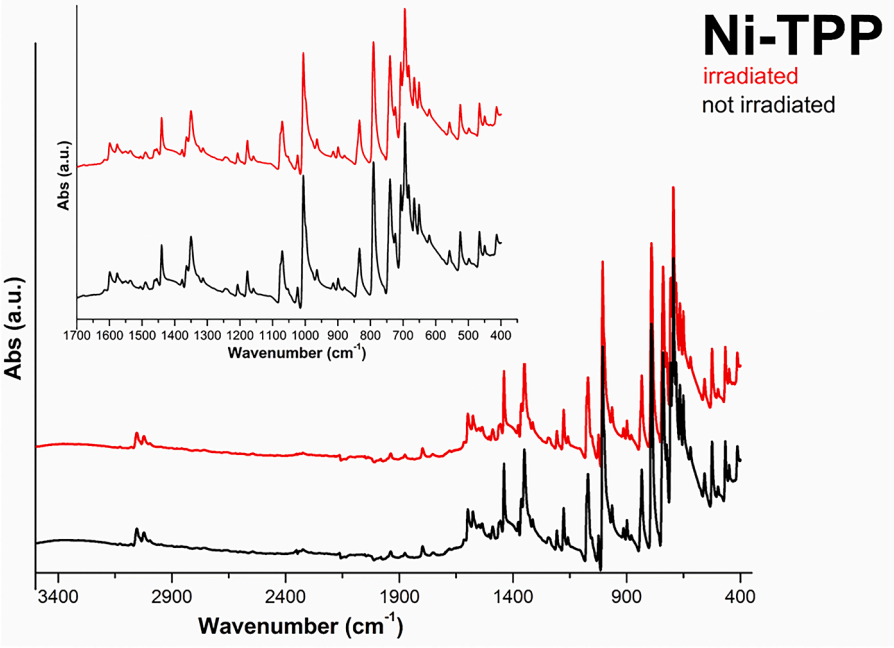

Fig. 3. ATR-FTIR spectra of Ni-TPP before (back) and after (red) irradiation with the 1.907 μm Raman Shifted radiation of a Nd:YAG pulsed laser. The details of the 1700-400 zone are shown in the upper left of the figure.

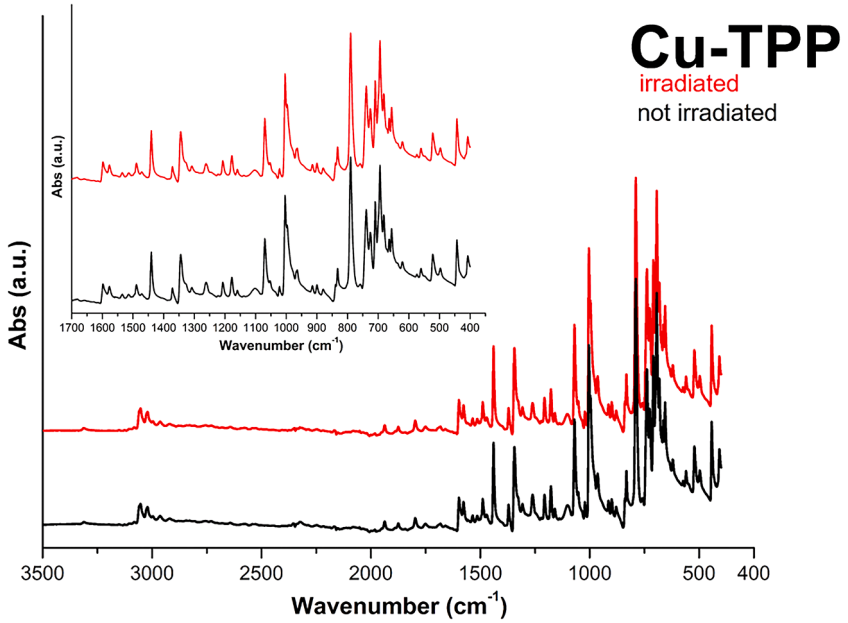

Fig. 4. ATR-FTIR spectra of Cu-TPP before (black) and after (red) irradiation with the 1.907 μm Raman Shifted radiation of a Nd:YAG pulsed laser. The details of the 1700-400 zone are shown in the upper left of the figure.

show a significant increase in magnetic moment, starting from an initial diamagnetic condition and reaching values between 5.16 and 6.28 BM (Bohr Magnetons). This behavior is similar to what was observed for the Co-TPP compound, which showed an increase in magnetic moment from pre-irradiation to post-irradiation from 2.0÷2.8 BM to 5.3÷8.2 BM.

Measurements carried out at regular time intervals, both for Co-TPP and Ni-TPP, have shown that the magnetic property is conserved over time, as is the enhancement of the SH emission. These results demonstrate that during the laser irradiation of the samples, a change of the spin state takes place for both complexes, *i. e.* they are excited into a high-spin or higher electronic state, maintaining this condition over time.

The situation of Cu-TPP is different. Also in this case we performed measures before and after irradiation in order to determine the magnetic moment, but we noticed that the magnetic moment did not change. The values are lying between 2.75 and 2.05 BM for every samples. This is consistent with the reported data [49], which attributed to Cu-TPP the doublet spin state. Thus, in the case of Cu-TPP, we do not observe a change of the spin state after the exposure to the laser. These results lead us to hypothesize that the enhancement of the SH signal is not necessarily connected to an increase in the magnetic moment.

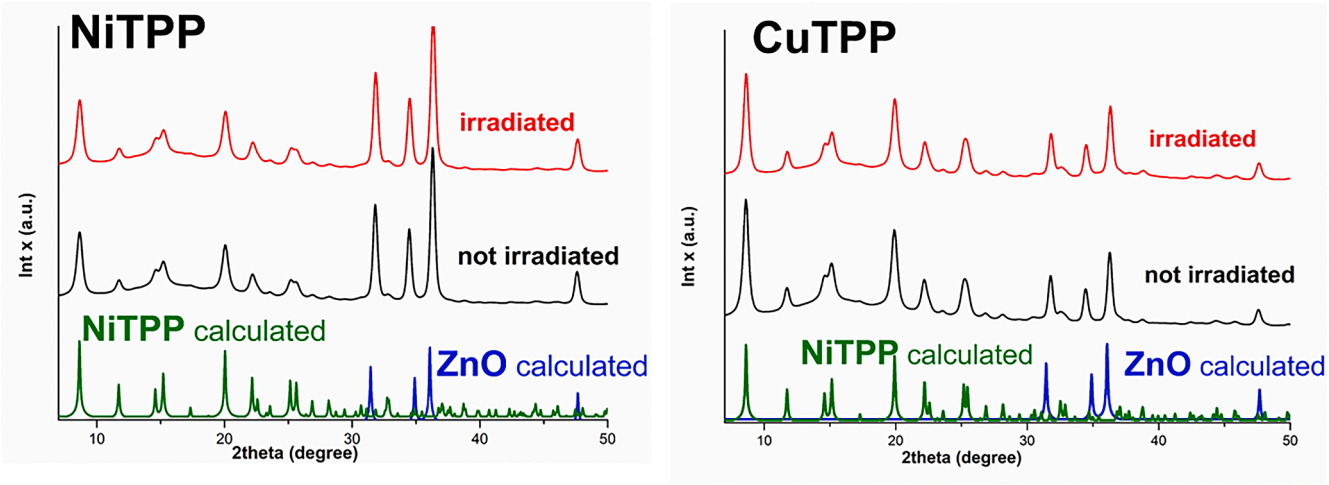

Fig. 5. XRPD patterns of powders of Ni/Cu-porphyrinates before and after irradiation with the Nd:YAG pulsed laser, mixed with those of ZnO, compared to the XRPD patterns calculated from the XRD structure, and to the ZnO pattern calculated for the P63mc structure from the ICSD databank (ZnOcalc). The patterns of the Ni/CuTPP powders were scaled on the peaks' intensity of ZnO.

3.5. EPR

EPR spectrum of Cu-TPP recorded at room temperature (RT) showed the typical axial pattern of a Cu(II) ion complex in a square planar geometry with d_{x2-y2} ground state and the spectral parameters, obtained by simulation of the experimental spectrum, ($g_{//} = 2.19$; $g_{\perp} = 2.05$ $A_{//} =$ 208 Gs; $A_{\perp} = 38$ Gs) are in agreement with the literature [49]. Moreover, as reported in Fig. 6, no spectral changes were observed after irradiation, in accordance with the unchanged values of the magnetic moment obtained with the magnetic balance.

Analogous experiments with Ni-TPP did not reveal any EPR signal, as expected from a diamagnetic system, both before and after irradiation. In this case, however, it should be noted that the increase in the value of the magnetic moment observed at the magnetic balance does not give rise to transitions observable at the EPR, neither at RT nor at 77 K.

3.6. Computational results

In order to perform theoretical calculations, small fragments of Ni-TPP and Cu-TPP were selected starting from the X-ray structures. These fragments are composed of two rings, cut from the crystallographic structures (Fig. 7).

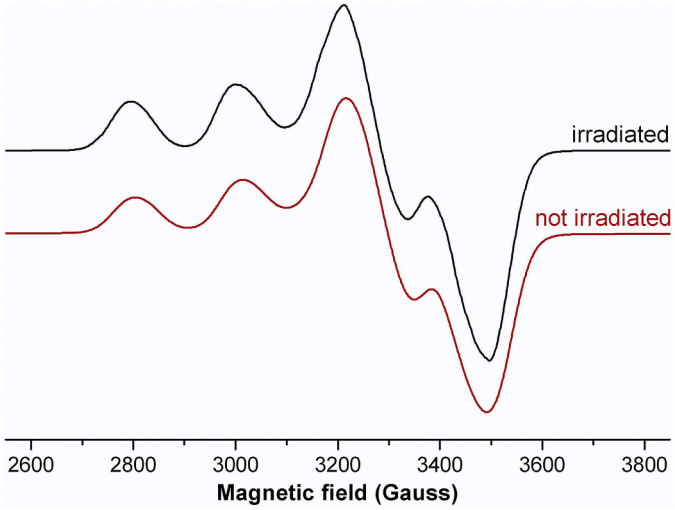

Fig. 6. EPR spectra at RT of Cu-TPP before and after irradiation.

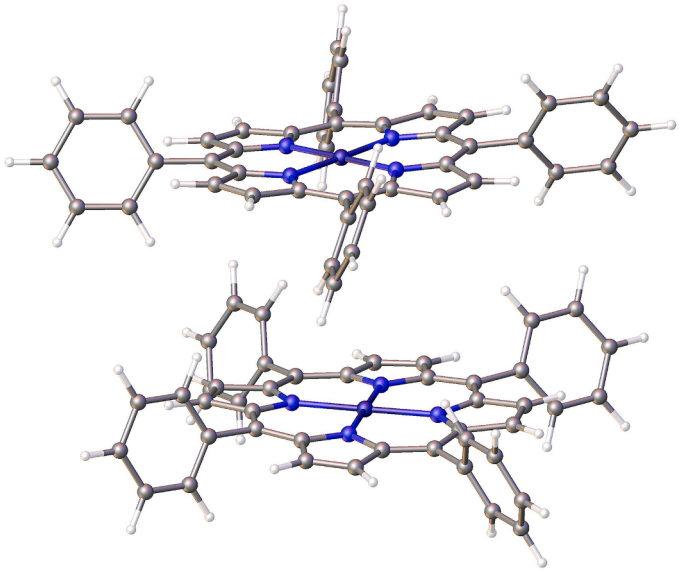

Fig. 7. Fragment of M-TPP (*M*=Ni, Cu) composed of two porphyrinate rings selected from the X-ray structures.

For both fragments, calculations were performed on the spin state (singlet for Ni-TPP and doublet for Cu-TPP), suggested by the experimental data [50]. The Cartesian coordinates of both fragments are reported in the Supplementary materials (Tables S3 and S4). Since sucrose is the reference compound for the SHG measurements, the same type of calculations was carried out also on a model of sucrose, composed of four sucrose units selected from the crystal structure downloaded from the Cambridge Structural Databank [51].

In Tables 1 and 2 are reported the theoretical geometrical parameters around the metal atom, compared to the corresponding XRD parameters. The bond differences between the XRD structures and the theoretically optimized geometries, are small and range from 0.03 Å for the Ni-N bond in Ni-TTP to a maximum of 0.06 Å for the Cu-N bond in Cu-TTP. About the bond angles, for Ni-TPP they are very similar to the experimental data and the maximum difference is about 0.12° for the angles N-Ni-N, while for Cu-TTP some differences are greater than one degree for the N-Cu-N angles.

In Table 3 are reported the root mean-square deviations (RMSD),

Table 1
Relevant distances (Å) around the metal atom for Ni-TPP and Cu-TPP from X-ray data and B3LYP/6–31G(d) calculations. All theoretical distances are averaged for the chemically equivalent bonds of the fragments.

	Ni-TPP (XRD)	Ni-TPP (B3LYP)	Cu-TPP (XRD)	Cu-TPP (B3LYP)
M-N1	1.93(1)	1.961	1.970(6)	2.027
M-N1[1]	1.93(1)	1.961	1.970(6)	2.030
M-N1[2]	1.93(1)	1.961	1.970(6)	2.030
M-N1[3]	1.93(1)	1.962	1.970(6)	2.027

1 (2-X,1-Y,+Z
2 (1/2+Y,3/2-X,3/2-Z)
3 (3/2-Y,-1/2+X,3/2-Z)

Table 2
Relevant bond angles (degree) around the metal atom for Ni-TPP and Cu-TPP from X-ray data and B3LYP/6–31G(d) calculations. All theoretical angles are averaged for the chemically equivalent bonds of the fragments.

	Ni-TPP (XRD)	Ni-TPP (B3LYP)	Cu-TPP (XRD)	Cu-TPP (B3LYP)
N1[1]-M-N1[2]	179.7(7)	179.67	178.4(5)	179.70
N1[2]-M-N1	90.000(5)	90.00	90.011(7)	90.06
N1[1]-M-N1[3]	90.000(3)	90.03	90.011(9)	89.98
N1[3]-M-N1	179.7(7)	179.82	178.4(5)	179.61
N1[1]-M-N1	90.000(6)	90.00	90.011(9)	89.87
N1[2]-M-N1[3]	90.001(4)	90.00	90.010(7)	90.16

1 (2-X,1-Y +Z)
2 (3/2-Y,-1/2+X,3/2-Z)
3 (1/2+Y,3/2-X,3/2-Z)

Table 3
Root mean square deviations RMSD (Å) of the atomic positions with respect to the mean plane of the porphyrin ring for Ni-TPP and Cu-TPP fragments. For the B3LYP geometries the values of both porphyrinate molecules are reported.

	Ni-TPP	Cu-TPP
B3LYP	0.243 - 0.246	0.156 - 0.155
XRD	0.272	0.229

calculated with the Olex2 software, of the atomic positions of the porfirinate ring with respect to the mean plane of the ring (that includes all N and C atoms, except those of the phenyl rings) both in the optimized fragments, and obtained from XRD structure. As it can be observed, for Ni-TPP the RMSD is very close to the experimental value, while for Cu-TPP the calculation provides a little more planar structure. Effectively, in the Ni-TPP theoretical geometry the Ni-N bond distances are very close to the experimental data (see Table 1) and thus the calculated Ni-TPP molecules show substantially ruffled porphyrin cores. Instead, for Cu-TPP the calculated Cu-N bond distances are slightly longer than the experimental ones (see Table 1) and the porphyrin cores result more planar. These results are consistent with what was already observed for the Co-TPP, *i.e.* the greater is the length of the M-N bond, the greater is the deviation from planarity of the porphyrin core.

To validate better our model, we compared the IR theoretical spectra obtained by analytical frequency calculations with the experimental ATR-FTIR spectra (already discussed in Section 3.3). The positions and assignments of the principal bands are reported in Tables 4 and 5. Figs. 8 and 9 show the theoretical spectra compared to the experimental ones. All the data were normalized with respect to the highest peaks, and no convolution was applied to the theoretical data. As can be seen, all the expected bands (see Section 3.3) were found. Minor differences in relative intensities and positions are attributable to the simplicity of the model. The only notable differences are found in the band attributable to the C-H stretching of the phenyl groups, which ranges between 3181 and 3216 cm^{-1} instead of between 3027 and 3052 cm^{-1} for Ni-TPP. In the corresponding Cu-TPP model, the C-H stretching band ranges between 3182 and 3216 cm^{-1} instead of 3019–3059 cm^{-1}. However, it is important to bear in mind that the spectra are calculated by using the harmonic approximation, and it is well known that mainly the high-frequency vibrations are affected by anharmonicity [46].

Table 4
Assignments of the principal vibrational bands, ATR-FTIR compared with the B3LYP/6–31G(d) model, for Ni-TPP.

NiTPP		
ATR-FTIR (cm^{-1})	B3LYP/6–31G(d) (cm^{-1})	Assignment
413–466	418.65–474.87	*In-plane rotational motion of the pyrrole rings, including wagging of the phenyl groups*
517–557	510.75–581.01	*Out-of-plane skeletal deformation of the phenyl groups,*
650–695	634.8–653.20	*Expansion of the phenyl groups*
710–725	714.90 – 742.60	*Wagging of the H atoms of the phenyl groups*
740–834	751.87–817.08	*Wagging of H atoms on the phenyl rings and macrocycle, including twisting of the macrocycle*
1006	1016.90–1017.78	*In-plane bending deformation of the phenyl rings*
1077	1070.19–1070.80	*Rocking of the H atoms on the C atoms on the ring*
1350	1344.25–1350.96	*In-plane structural deformation of the pyrrole*
1440	1412.73–1412.72	*Rocking of the H atoms on the phenyl rings and symmetric C—C-C bond stretching*
3027 - 3052	3181.79–3215.81	*C-H stretching of phenyl*

Table 5
Assignments of the principal vibrational bands, ATR-FTIR compared with the B3LYP/6–31G(d) model, for Cu-TP.

CuTPP		
ATR-FTIR (cm^{-1})	B3LYP/6–31G(d) (cm^{-1})	Assignment
408–443	412.36–414.38	*In-plane rotational motion of the pyrrole rings, including wagging of the phenyl groups*
521–560	568.97–576.52	*Out-of-plane skeletal deformation of the phenyl groups,*
656	651.35–651.85	*Expansion of the phenyl groups*
710 -739	715.13–781.32	*Wagging of the H atoms of the phenyl groups*
832	806.09–859.64	*Wagging of H atoms on the phenyl rings and macrocycle, including twisting of the macrocycle*
1004	1016.58–1017.52	*In-plane bending deformation of the phenyl rings*
1069	1036–1044.74	*Rocking of the H atoms on the C atoms on the ring*
1344	1300.24–1318.63	*In-plane structural deformation of the pyrrole*
1440	1485.44–1490.30	*Rocking of the H atoms on the phenyl rings and symmetric C—C-C bond stretching*
3019–3059	3182.24–3215.11	*C-H stretching of phenyl*

In Table 6 are reported all fragments' computed values of the dipole moment μ, the mean polarizability α, and an estimate of the intrinsic molecular hyperpolarizability (β) in absence of any resonance effect represented by a third rank tensor. The twenty-seven components of the 3D matrix can be reduced to ten components according to Kleinman symmetry. The Gaussian16 output file provides the main ten components (β_{xxx}, β_{xxy}, β_{xyy}, β_{yyy}, β_{xxz}, β_{xyz}, β_{yyz}, β_{xzz}, β_{yzz}, and β_{zzz}), whose values for the studied compounds are reported in Supplementary materials (Tables S7 and S8). The magnitude of the total first hyperpolarizability (β_{tot}) can be defined as,

$$\beta_{tot} = \sqrt{\left(\beta_{xxx} + \beta_{xyy} + \beta_{xzz}\right)^2 + \left(\beta_{xxy} + \beta_{yyy} + \beta_{yzz}\right)^2 + \left(\beta_{xxz} + \beta_{zyy} + \beta_{zzz}\right)^2} \quad (1)$$

The relationship between the macroscopic second-order

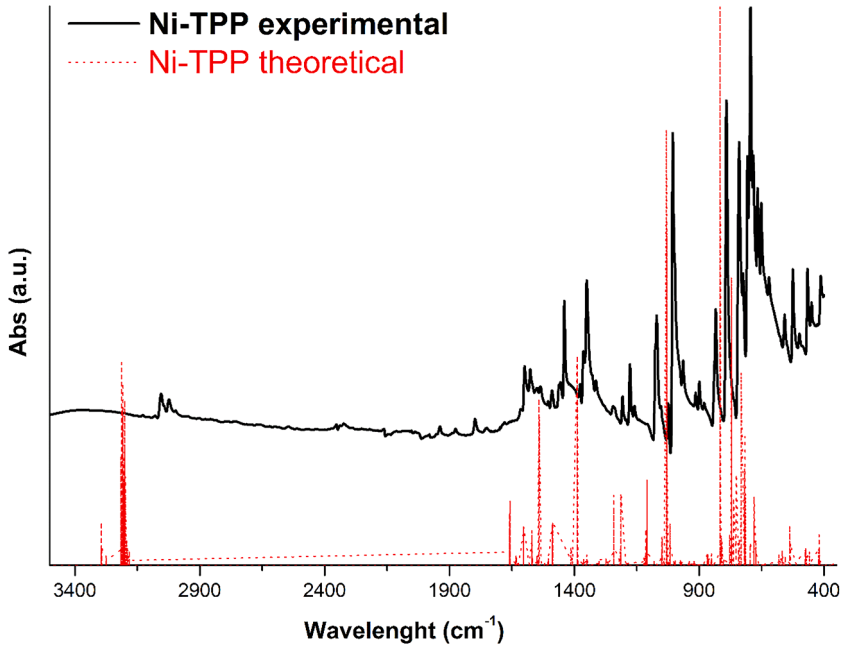

Fig. 8. ATR-FTIR spectrum of Ni-TPP (black line) compared with theoretical data (red dotted line).

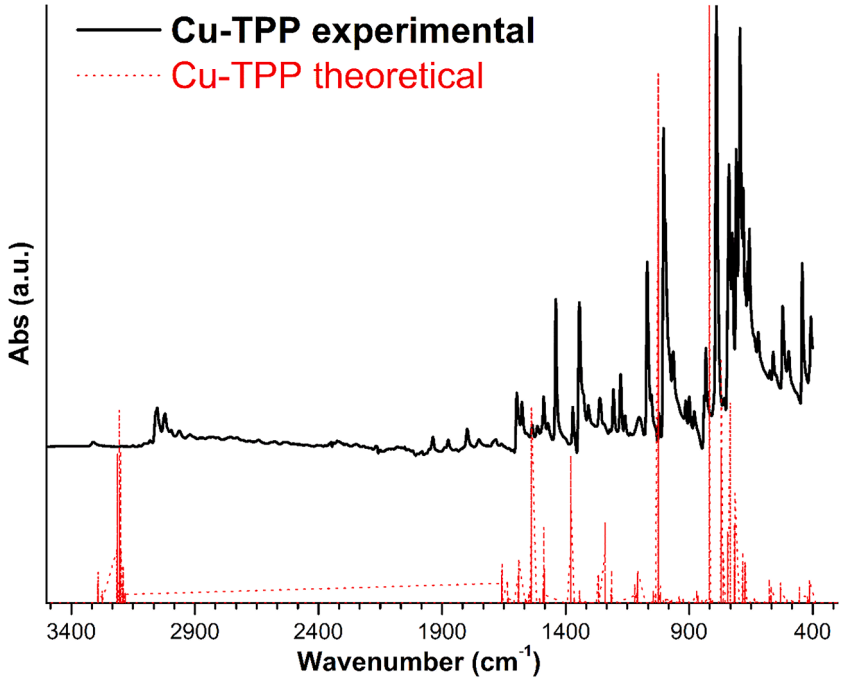

Fig. 9. ATR-FTIR spectrum of Cu-TPP (black line) compared with theoretical data (red dotted line).

Table 6
Computed dipole moments μ (Debye), mean polarizabilities ⟨α⟩ (a.u.), first static hyperpolarizabilities β_{tot} (10^{-30} cm^5 esu^{-1}), second order susceptibilities $\chi^{(2)}$ (pm V^{-1}), second order susceptibilities ratios with respect to sucrose values.

	Ni-TPP	Cu-TPP
μ	0.0208	0.5012
<α>	1238	1253
β_{tot}	0.2	1.3
$\chi^{(2)}$	0.0(4)	0.2
$\chi^{(2)}/\chi^{(2)}_{sucrose}$	0.0(2)	0.1

susceptibility, the quantity correlated to the second harmonic intensity, and the microscopic hyperpolarizability is given by the following equation [52]:

$$\chi^{(2)} = \beta NF \quad (2)$$

where N is the number of particles per unit volume and F is the local field factor. F depends upon the crystal symmetry and is related to the crystal's refractive index. Values between 1 and 2 are generally reported and, in particular for saccharides, this value range between 1.5 and 1.6 [53].

Since our interest is focused on the trend of the ratio $\chi^{(2)}/\chi^{(2)}_{sucrose}$, we

assumed $F = 1$. The ratios between the second-order susceptibility of the compounds and that of sucrose is also reported, together with the ratios between the corresponding SHG intensities, in order to compare the computational results with the experimental measurements.

Both M-TPP fragments have rather high polarizability values, but very low hyperpolarizability and optical susceptibility, as already observed for Co-TPP in our previous work. In particular, Ni-TPP shows values of dipole moment, hyperpolarizability and optical susceptibility very close to zero, while the optical susceptibility value of Cu-TPP is 0.1 with respect to the standard. However, the ratios of optical susceptibility with respect to sucrose are all extremely low. These results are in agreement with the experimental SHG efficiencies of Ni-TPP and Cu-TPP before the irradiation with the laser.

Considering the results obtained from the magnetic balance for the irradiated Ni-TPP, we performed the geometry optimizations at the B3LYP/6–31G(d) on the same fragment showed in Fig. 7 in different spin excited states. Thus, we evaluated the variation of the hyperpolarizability (β) as a function of the number of unpaired electrons of the system. The resulted main geometrical parameters are shown in Tables 7 and 8, and the values of the dipole moment, polarizability and hyperpolarizability as a function of the number of unpaired electrons are shown in Table 9. All geometrical parameters and all components of vectors and tensors are reported in Supplementary materials (Tables S5, S6, S9, S10). The geometrical parameters of the excited spin states (Tables 7 and 8) are very similar to the geometry of the ground state (Tables 1 and 2), in agreement with the experimental XRPD data that do not detect structural changes for the irradiated sample. Instead, the polarizability values (Table 9) show small changes as a function of the spin state, and the dipole moments changes by an order of magnitude from 0 to 2 or 4 unpaired electrons. On the contrary, for the Co-TPP both the dipole moment and the polarizability values slightly changed as a function of the spin state. Furthermore, for the Ni-TPP the hyperpolarizability changes by an order of magnitude from 0 to 2, and increases by a further order of magnitude from 2 to 4 unpaired electrons. This is coherent with what previously observed in Co-TPP, for which the hyperpolarizability changes by an order of magnitude from 2-3 to 4-5 unpaired electrons. These results are in agreement with the experimental data of the magnetic balance, in which the irradiated sample has a high SHG emission and a rather high magnetic moment, compatibly to the excited spin states.

TDDFT calculations were performed on both Ni-TPP and Cu-TPP in the ground state, in order to calculate the UV–Vis spectra to compare with the experimental ones recorded in the solid state. As shown in Tables 10 and 11, the theoretical and experimental UV–Vis spectra are in good agreement. In the theoretical spectrum of Ni-TPP (Table 10), in the range 711–718 nm there are forbidden transitions ($f = 0$), associated to a change in the spin. As already reported, these theoretical transitions are all at zero oscillator strength, but actually in the experimental spectra we found a low intensity transition (722 nm), visible both before and after laser radiation (see Fig. 1). This is coherent with the results found for Co-TPP, already discussed. These results lead us to think that all these spin forbidden transitions can occur, and that they are permanent.

Table 7
Relevant distances (Å) around the metal atom for Ni-TPP in different spin excited states, calculated at the B3LYP/6–31G(d) level. The number of unpaired electrons in the fragments is given in columns. All theoretical distances are averaged for the chemically equivalent bonds of the fragments.

Ni-TPP	XRD	0	2	4
M-N1[1]	1.93(1)	1.961	1961	2012
M-N1[2]	1.93(1)	1.961	1961	2008
M-N1	1.93(1)	1.961	1961	2010
M-N1[3]	1.93(1)	1.962	1961	2007

[1] (2-X,1-Y,+Z)
[2] (1/2+Y,3/2-X,3/2-Z)
[3] (3/2-Y,-1/2+X,3/2-Z)

Table 8
Relevant bond angles (degree) around the metal atom for Ni-TPP in different spin excited states calculated at the B3LYP/6–31G(d) level. The number of unpaired electrons in the fragments is given in columns. All theoretical angles are averaged for the chemically equivalent bonds of the fragments.

Ni-TPP	XRD	0	2	4
N1[1]-M1-N1[2]	179.7(7)	179,73	179,73	179,49
N1[2]-M1-N1	90.000(5)	90,01	89,98	90,04
N1[1]-M1-N1[3]	90.000(3)	89,98	90,01	89,95
N1[3]-M1-N1	179.7(7)	179,74	179,74	179,69
N1[1]-M1-N1	90.000(6)	90,03	89,98	89,94
N1[2]-M1-N1[3]	90.001(4)	89,98	90,06	90,06

[1] (2-X,1-Y, +Z)
[2] (3/2-Y,-1/2+X,3/2-Z)
[3] (1/2+Y,3/2-X,3/2-Z)

Table 9
Dipole moments μ (Debye), mean polarizabilities ⟨α⟩ (a.u.), first static hyperpolarizabilities βtot (10^{-30} cm^5esu^{-1}) computed for Ni-TPP on optimized geometries of fragments with several excited spin states (0 unpaired electrons, 2 unpaired electrons and 4 unpaired electrons).

	0	2	4
μ	0.0208	0.4382	0.3479
<α>	1239	1230	1263
β_{tot}	0.2	3.1	24.5
$\chi^{(2)}$	0.0(4)	0,6	4,7
$\chi^{(2)}/\chi^{(2)}_{sucrose}$	0.0(2)	0,4	3,4

Table 10
Theoretical and experimental electronic transitions (nm) for Ni-TPP. The width of the bands is reported in parenthesis.

Ni-TPP	Experimental	Theoretical
Soret bands	358 (348–368)	375 (350–376)
	515	385 (380–399)
Q bands	519 (505–560)	523
	619	(592–601)
	655	644
	722	(711–718)

Table 11
Theoretical and experimental electronic transitions (nm) for Cu-TPP. The width of the bands is reported in parenthesis.

Cu-TPP	Experimental	Theoretical
Soret bands	349 (349–374)	377 (343–380)
	469 (457–476)	391 (385–404)
Q bands	533 (522–558)	522–539
	623 (604–638)	573–612
	657 (649–662)	668–740
	821 (803–837)	786–788

Different is the situation for the Cu-TPP. As reported in Sections 3.5 and 3.6, this complex doesn't show any change of the magnetic moment or magnetic behavior, and thus we do not expect transitions associated with a change in the spin, that could explain an exited state induced by the laser radiation. In the theoretical spectra of Cu-TPP (Table 11), we found forbidden transitions in the range 786–788 nm. These transitions are also present in the experimental spectra in the range 803–837 nm (see Fig. 2), with low intensity peaks, both in the spectrum recorded before and after laser irradiation (821 nm).

In Fig. 10 is reported the plot of the molecular orbitals principally involved in the transition found at 788 nm. This transition shows oscillator strength equal to zero ($f = 0$), and a value of the operator S^2 equal to 2.018, consistent with a doublet, that is the ground state of Cu-TPP. In this transition, the mainly involved orbitals are the 337B

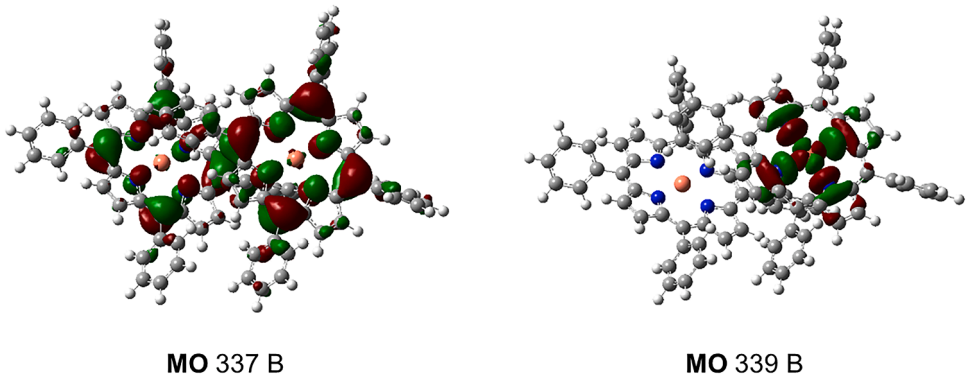

Fig. 10. Plot of the molecular orbitals (MO) principally involved in the forbidden transition found at 788 nm. The 337B is the starting MO, and the 339B is the arriving MO.

(starting MO) and the 339B (arriving MO). As we can see in the figure, the starting molecular orbital is principally constituted by π orbitals of the ligand, and in the arriving molecular orbital there is a big contribution of the metal d orbitals.

The plots of all the molecular orbitals mainly involved in the transitions at 788 nm are reported in the Supplementary materials (section IV). By visualizing these plots, it is possible to see that all the forbidden transition follow the same scheme showed in Fig. 10. Therefore in all these transitions we observe a change in the electronic distribution of the orbitals, consistent with a charge transfer, previously observed for metal porphyrinates [54].

4. Conclusions

The aim of this study was to analyze the Second Harmonic Generation (SHG) behavior of Nickel(II)- and Copper(II)-5,10,15,20-tetraphenylporphyrin complexes in the solid state, that are isomorphous of the analogue Cobalt porphyrinato, and exhibit a significant increase in the SHG efficiency during laser irradiation that persists over time, as previously observed for Co-TPP. The optical characterization through UV–Vis spectroscopy, both in solution and the solid state, coupled with the solid-state IR spectroscopy, ruled out the possibility of a photodegradation processes, while XRPD experiments excluded phase transitions or partial amorphizations of the samples. The magnetic susceptibility measurements and the EPR spectra provided additional insights: the Ni-TPP shows a significant increase in the magnetic moment after irradiation, corresponding to a substantial change in the spin state of the sample, as observed for the analogous Co-TPP. On the contrary, the Cu-TPP remains stable in terms of magnetic properties. The EPR results are consistent with those of the magnetic balance for Cu-TPP, while, surprisingly, for Ni-TPP the value of the magnetic moment observed at the magnetic balance does not give rise to transitions observable at the EPR, neither at RT nor at 77 K. Thus, the SHG behavior is not correlated to changes in the magnetic moment.

The theoretical calculations, performed on Ni-TPP and Cu-TPP fragments, simulate the structural features of the complexes and their initial experimental SHG responses. The optimization of the Ni-TPP fragment with higher spin multiplicities yields higher hyperpolarizability values, and in particular the increase in hyperpolarizability is related to the enhance of unpaired electrons. Thus, these results support the proposed hypothesis in our previous work on Co-TPP: the enhancement of the SHG efficiencies of the metal-porphyrinates is attributable to an electronic or a spin transition, that occurs when they are irradiated.

Theoretical UV–Vis spectra obtained from TDDFT calculations revealed forbidden transitions for both Ni-TPP and Cu-TPP. In the case of Ni-TPP, these transitions are spin-forbidden, in agreement with the change of the spin state observed experimentally after irradiation. In the case of Cu-TPP the transitions are symmetry-forbidden, again in agreement with the experimental data.

In the UV–Vis spectra obtained experimentally from the powders of both samples, low intensity transitions are observed in the same range as those obtained theoretically. This supports the proposal of reaching a stable excited state over time following laser irradiation.

CRediT authorship contribution statement

Alma Cioci: Writing – review & editing, Writing – original draft, Validation, Supervision, Software, Resources, Project administration, Methodology, Investigation, Formal analysis, Data curation, Conceptualization. **Paola Antoniotti:** Writing – review & editing, Writing – original draft, Visualization, Validation, Supervision, Software, Resources, Project administration, Methodology, Investigation, Formal analysis, Data curation, Conceptualization. **Paola Benzi:** Writing – review & editing, Visualization, Resources, Project administration, Investigation, Formal analysis, Data curation. **Carlo Canepa:** Writing – review & editing, Validation, Resources, Investigation, Data curation. **Elena Cariati:** Writing – review & editing, Validation, Resources, Investigation, Data curation. **Enzo Laurenti:** Writing – review & editing, Validation, Resources, Investigation, Data curation. **Domenica Marabello:** Writing – review & editing, Writing – original draft, Validation, Supervision, Resources, Project administration, Methodology, Investigation, Formal analysis, Data curation, Conceptualization.

Declaration of competing interest

The authors declare that they have no known competing financial interests or personal relationships that could have appeared to influence the work reported in this paper.

Data availability

Data will be made available on request.

Acknowledgments

Financial support from NextGenerationEU (PRIN-2022KHEZTC).

For diffuse reflectance UV–Vis spectra and Attenuated total Reflectance-Fourier-Transform-Infrared (ATR-FTIR) we thank the company 2D TO 3D S.r.l.s.

Supplementary materials

Supplementary material associated with this article can be found, in the online version, at doi:10.1016/j.molstruc.2024.139201.

References

[1] W.R. Zipfel, R.M. Williams, W.W. Webb, Nonlinear magic: multiphoton microscopy in the biosciences, Nat. Biotech. 21 (2003) 1369–1377.
[2] L. Moreaux, O. Sandre, M. Blanchard-Desce, J. Mertz, Membrane imaging by simultaneous second-harmonic generation and two-photon microscopy, Opt. Lett. 25 (2000) 320–322.
[3] P.J. Campagnola, et al., Three-dimensional high-resolution second-harmonic generation imaging of endogenous structural proteins in biological tissues, Biophys. J. 81 (2002) 493–508.
[4] M.J. Therien, How to improve your image, Nature 458 (7239) (2009) 716–717.
[5] L. Sacconi, D.A. Dombeck, W.W. Webb, Overcoming photodamage in second-harmonic generation microscopy: real-time optical recording of neuronal action potentials, Proc. Natl Acad. Sci. U. S. A. 103 (2006) 3124–3129.
[6] W.P. Dempsey, S.E. Fraser, P. Pantazis, SHG nanoprobes: advancing harmonic imaging in biology, BioEssays 34 (5) (2012) 351–360.
[7] A. Kachynski, A. Kuzmin, M. Nyk, I. Roy, et al., Zinc oxide nanocrystals for non-resonant nonlinear optical microscopy in biology and medicine, J. Phys. Chem. C 112 (2008) 10721–10724.
[8] T.R. Kuo, C.L. Wu, C.T. Hsu, W. Lo, et al., Chemical enhancer induced changes in the mechanisms of transdermal delivery of zinc oxide nanoparticles, Biomaterials 30 (2009) 3002–3008.
[9] C.L. Hsieh, R. Grange, Y. Pu, D. Psaltis, Three-dimensional harmonic holographic microcopy using nanoparticles as probes for cell imaging, Opt Express 17 (2009) 2880–2891.
[10] J. Extermann, L. Bonacina, E. Cuña, C. Kasparian, et al., Nanodoublers as deep imaging markers for multi-photon microscopy, Opt. Express 17 (2009) 15342–15349.
[11] P. Pantazis, J. Maloney, D. Wu, S.E. Fraser, Second harmonic generating (SHG) nanoprobes for *in vivo* imaging, Proc. Natl. Acad. Sci. U. S. A. 107 (2010) 14535–14540.
[12] G. Pandey, R. Chaudhari, B. Joshi, S. Choudhary, J. Kaur, A. Joshi, Fluorescent biocompatible platinum-porphyrin–doped polymeric hybrid particles for oxygen and glucose biosensing, Sci. Rep. 9 (2019) 5029–5040.
[13] K. Norvaiša, M. Kielmann, M.O. Senge, Porphyrins as Colorimetric and photometric biosensors in modern bioanalytical systems, ChemBioChem 21 (2020) 1–16.
[14] M. Imran, M. Ramzan, A.K. Qureshi, M.A. Khan, M. Tariq, Emerging applications of porphyrins and metalloporphyrins in biomedicine and diagnostic magnetic resonance imaging, Biosensors 8 (2018) 95–111.
[15] S. Chandra, C. Mende, D. Bahadur, A. Hildebrandt, H. Lang, Fabrication of a porphyrin-based electrochemical biosensor for detection of nitric oxide released by cancer cells, J. Solid State Electrochem. 19 (2015) 169–177.
[16] X. Liu, D. Wang, H. Gao, Z. Yang, Y. Xing, H. Cao, W. He, H. Wang, J. Gu, H. Hu, Nonlinear optical properties of symmetrical and asymmetrical porphyrin derivatives with click chemistry modification, Dyes Pigments 134 (2016) 155–163.
[17] K. De Mey, K. Clays, M.J. Therien, D.N. Beratan, I. Asselberghs, Analysis of the unusual wavelength dependence of the first hyperpolarizability of porphyrin derivatives, Proc. SPIE (2010) 777403, https://doi.org/10.1117/12.859819. Linear and Nonlinear Optics of Organic Materials X.
[18] G. Di Carlo, M. Pizzotti, S. Righetto, A. Forni, F. Tessore, Electric-field-induced second harmonic generation nonlinear optic response of A4 β-pyrrolic-substituted ZnII porphyrins: when cubic contributions cannot be neglected, Inorg. Chem. 59 (11) (2020) 7561–7570.
[19] B. Li, P. Sathishkumar, F.L. Gu, C. Zhu, Insight into the expanded mislinked porphyrins with high second order nonlinear optical response, J. Phys. Chem. A 124 (5) (2020) 955–965.
[20] K. Sendhil, C. Vijayan, M.P. Kothiyal, Nonlinear optical properties of a porphyrin derivative incorporated in Nafion polymer, Opt. Mater. 27 (2005) 1606–1609. Amst.
[21] A. Khadria, J. Fleischhauer, I. Boczarow, J.D. Wilkinson, M.M. Kohl, H. L. Anderson, Porphyrin dyes for nonlinear optical imaging of live cells, iScience 4 (2018) 153–163.
[22] J.E. Reeve, H.A. Collins, K.D. Mey, M.M. Kohl, K.J. Thorley, O. Paulsen, K. Clays, H.L. Anderson, Amphiphilic porphyrins for second harmonic generation imaging, J. Am. Chem. Soc. 131 (8) (2009) 2758–2759.
[23] Y.R. Shen, The Principles of Nonlinear Optics, Wiley, New York, 1984.
[24] P. Antoniotti, C. Canepa, E. Cariati, A. Cioci, E. Laurenti, D. Marabello, G. Volpi, P. Benzi, The peculiar SHG behaviour of Co-5, 10, 15, 20-tetraphenilporphyrinate in the solid state. An experimental and theoretical study, J. Mol. Struct. 1294 (2023) 136340.
[25] G.S. Girolami, T.B. Rauchfuss, R.J. Angelici, Synthesis and Technique in Inorganic Chemistry, 3rd ed., University Science Books, Melville, NY, 1999. ISBN 978-0-935702-48-4.
[26] CrysAlisPro (2014). Agilent technologies, version 1.171.37.31 (release 14-01-2014 CrysAlis171. NET, compiled Jan 14 2014,18:38:05.
[27] G.M. Sheldrick, SHELXT-integrated space-group and crystal-structure determination, Acta Crystallogr. A 71 (2015) 3–8.
[28] G.M. Sheldrick, Crystal structure refinement with SHELXL, Acta Crystallogr. C 71 (2015) 3–8.
[29] O.V. Dolomanov, L.J. Bourhis, R.J. Gildea, J.A.K. Howard, H. Puschmann, Complete structure solution, refinement and analysis program, J. Appl. Crystallogr. 42 (2009) 339–341.
[30] Gaussian 16, Revision C.01, M.J. Frisch, G.W. Trucks, H.B. Schlegel, G.E. Scuseria, M.A. Robb, J.R. Cheeseman, G. Scalmani, V. Barone, G.A. Petersson, H. Nakatsuji, X. Li, M. Caricato, A.V. Marenich, J. Bloino, B.G. Janesko, R. Gomperts, B. Mennucci, H.P. Hratchian, J.V. Ortiz, A.F. Izmaylov, J.L. Sonnenberg, D. Williams-Young, F. Ding, F. Lipparini, F. Egidi, J. Goings, B. Peng, A. Petrone, T. Henderson, D. Ranasinghe, V.G. Zakrzewski, J. Gao, N. Rega, G. Zheng, W. Liang, M. Hada, M. Ehara, K. Toyota, R. Fukuda, J. Hasegawa, M. Ishida, T. Nakajima, Y. Honda, O. Kitao, H. Nakai, T. Vreven, K. Throssell, J.A. Montgomery, Jr., J.E. Peralta, F. Ogliaro, M.J. Bearpark, J.J. Heyd, E.N. Brothers, K.N. Kudin, V.N. Staroverov, T.A. Keith, R. Kobayashi, J. Normand, K. Raghavachari, A.P. Rendell, J.C. Burant, S.S. Iyengar, J. Tomasi, M. Cossi, J.M. Millam, M. Klene, C. Adamo, R. Cammi, J.W.
[31] H.B. Schlegel, An efficient algorithm for calculating ab initio energy gradients using s, p Cartesian Gaussians, J. Chem. Phys. 77 (1982) (1982) 3676–3681.
[32] H.B. Schlegel, Optimization of equilibrium geometries and transition structures, J. Comput. Chem. 3 (1982) 214–218.
[33] H.B. Schlegel, C. Daudel, Computational Theoretical Organic Chemistry (1981) 129, edited by I. G. Csizsmadia and R. Daudel.
[34] A.D. Becke, Density-functional thermochemistry. III. The role of exact exchange, J. Chem. Phys. 98 (7) (1993) 5648–5652.
[35] A.D. Becke, Density-functional exchange-energy approximation with correct asymptotic behavior, Phys. Rev. A 38 (6) (1988) 3098–3100.
[36] W.J. Hehre, L. Radom, P.V. Schleyer, J.A. Pople, Ab Initio Molecular Orbital Theory, Wiley, New York, 1986.
[37] W.R. Wadt, P.J. Hay, Ab initio effective core potentials for molecular calculations. Potentials for the transition metal atoms Sc to Hg, J. Chem. Phys. 82 (1985) 270–283.
[38] D.F. Parsons, B.W. Ninham, Ab initio molar volumes and Gaussian radii, J. Phys. Chem. A 113 (6) (2009) 1141–1150, https://doi.org/10.1021/jp802984b. PMID19140766.
[39] R. Bauernschmitt, R. Ahlrichs, Treatment of electronic excitations within the adiabatic approximation of time dependent density functional theory, Chem. Phys. Lett. 256 (1996) 454–464, https://doi.org/10.1016/0009-2614(96)00440-X.
[40] R.E. Stratmann, G.E. Scuseria, M.J. Frisch, An efficient implementation of time-dependent density-functional theory for the calculation of excitation energies of large molecules, J. Chem. Phys. 109 (1998) 8218–8224, https://doi.org/10.1063/1.477483.
[41] GaussView, Version 6, Roy Dennington, Todd Keith, and John Millam, Semichem Inc., Shawnee Mission, KS, 2016.
[42] S.K. Kurtz, T.T. Perry, A powder technique for the evaluation of nonlinear optical materials, J. Appl. Phys. 39 (1968) 3798–3813.
[43] A.S. Davydov, Theory of Molecular Excitons, Springer, New York, NY, 1971, p. 313.
[44] E.G. McRae, M. Kasha, Enhancement of phosphorescence ability upon aggregation of dye molecules, J. Chem. Phys. 28 (1958) 721–722, https://doi.org/10.1063/1.1744225.
[45] M.M. El-Nahass, H.M. Zeyada, M.S. Aziz, M.M. Makhlouf, Optical absorption of tetraphenylporphyrin thin films in UV–Vis-NIR region, Spectrochim. Acta A Mol. Biomol. Spectrosc. 61 (2005) 3026–3031, https://doi.org/10.1016/j.saa.2004.11.022.
[46] M. Aydin, Comparative study of the structural and vibroelectronic properties of porphyrin and its derivatives, Molecules 19 (12) (2014) 20988–21021.
[47] M. Aydin, DFT and Raman spectroscopy of porphyrin derivatives: tetraphenylporphine (TPP), Vib. Spectrosc. 68 (2013) 141–152.
[48] M.S. Liao, S. Scheiner, Comparative study of metal-porphyrins,-porphyrazines, and-phthalocyanines, J. Comput. Chem. 23 (15) (2002) 1391–1403.
[49] C. Calle, A. Schweiger, G. Mitrikas, Continuous-wave and pulse EPR study of the copper(II) complex of N-confused tetraphenylporphyrin: direct observation of a sigma metal-carbon bond, Inorg. Chem. 46 (2007) 1847–1855, https://doi.org/10.1021/ic0621852.
[50] M.S. Liao, S. Scheiner, Electronic structure and bonding in metal porphyrins, metal=Fe,Co,Ni,Cu,Zn, J. Chem. Phys. 117 (2002) 205–218.
[51] CCDC: SUCROS04, G.M. Brown, H.A. Levy, Further refinement of the structure of sucrose based on neutron-diffraction data, Acta Crystallogr. Sect. B Struct. Crystallogr. Cryst. Chem. 29 (4) (1973) 790–797.
[52] R.W. Boyd, Nonlinear Optics, 3rd ed., Academic Press, Philadelphia, 2008. ISBN: 978-0-12-369470-6.
[53] R.R. Choudhury, R. Chitra, Investigation of hydrogen bond effects on the hyperpolarizability of 2-Aminopyridinium maleate (2APM) complex and determining the non-linear optical susceptibility of the molecular crystal of 2APM, Mol. Phys. 109 (13) (2011) 1701–1708, https://doi.org/10.1080/00268976.2011.587458.
[54] M.A. Naumova, G. Paveliuc, M. Biednov, K. Kubicek, A. Kalinko, J. Meng, M. Liang, A. Rahaman, M. Abdellah, S. Checchia, F.A. Lima, P. Zalden, W. Gawelda, C. Bressler, H. Geng, W. Lin, Y. Liu, Q. Zhao, Q. Pan, M. Akter, Q. Kong, M. Retegan, D.J. Gosztola, M. Pápai, D. Khakhulin, M.L. Daku, K. Zheng, S. E. Canton, Nonadiabatic charge transfer within photoexcited nickel porphyrins, J. Phys. Chem. Lett. 15 (2024) 3627–3638.